Article

# Synthesis and characterization of (Sn,Zn)O alloys

Andre Bikowski, Aaron Holder, Haowei Peng, Sebastian Siol, Andrew Norman, Stephan Lany, and Andriy Zakutayev

*Chem. Mater.*, **Just Accepted Manuscript** • DOI: 10.1021/acs.chemmater.6b02968 • Publication Date (Web): 29 Sep 2016

# Synthesis and characterization of (Sn,Zn)O alloys

Andre Bikowski[1], Aaron Holder[1], Haowei Peng[1], Sebastian Siol[1], Andrew Norman[1], Stephan Lany[1], Andriy Zakutayev[1]

[1]National Renewable Energy Laboratory, 15013 Denver West Parkway, Golden, Colorado 80401, USA

## Abstract

SnO exhibits electrical properties that render it promising for solar energy conversion applications, but it also has a strongly indirect band gap. Recent theoretical calculations predict that this disadvantage can be mitigated by isovalent alloying with other group-II oxides such as ZnO. Here, we synthesized new metastable isovalent (Sn,Zn)O alloy thin films by combinatorial reactive co-sputtering and characterized their structural, optical and electrical properties. The alloying of ZnO into SnO leads to a change of the valence state of the tin from $Sn^{0}$ via $Sn^{2+}$ to $Sn^{4+}$, which can be counteracted by reducing the oxygen partial pressure during the deposition. The optical characterization of the smooth <10 at. % $Sn_{1-x}Zn_xO$ thin films showed an increase in the absorption coefficient in the range from 1 to 2 eV, which is consistent with the theoretical predictions for the isovalent alloying. However, the experimentally observed alloying effect may be convoluted with the effect of local variations of the Sn oxidation state. This effect would have to be minimized to improve the (Sn,Zn)O optical and electrical properties for their use as absorbers in solar energy conversion applications.

## 1. Introduction

New absorber materials that can enable high energy conversion efficiency of sunlight to electricity without using "critical" elements are of great technological interest for solar energy conversion applications[1], such as photovoltaic[2] or photoelectrochemical[3] solar cells. These materials need to have a high optical absorption in the visible and infrared portion of the solar spectrum, high electrical charge carrier mobility and lifetimes, and controllable p- and n-type doping.[4] In particular, oxide absorbers are attractive due to the potential for the use of inexpensive precursor materials and scalable fabrication methods.[5] However, most oxides posses wide band gaps, large hole effective masses, and are either insulating or n-type, with very few exceptions. For these reasons, the use of oxides as absorbers in photovoltaics is relatively well established only for $Cu_2O$ (Ref. 6,7), with solar cells that have over 5% energy conversion efficiency. Recently, several new oxide absorber materials, such as $Co_3O_4$ (Ref. 8) and $Bi(Fe,Cr)O_3$ (Ref.9) have also been investigated for photovoltaic solar energy conversion applications. The range of studied oxide materials for photoelectrochemical solar cells is wider, including binaries (e.g. $TiO_2$[10], $WO_3$[11], $Fe_2O_3$[12]), and more recently ternaries (Bi-V-O[13], Mn-V-O[14], Cu-Si-Ti-O[15]), but the solar-to-hydrogen conversion efficiencies are generally lower.

The material discussed in this paper, tin monoxide (SnO), has layered litharge crystal structure (space group 129), yet an exceptionally low hole effective mass (~0.5 $m_0$)[16,17] comparable to conventional photovoltaic (PV) absorbers (Si, GaAs, CdTe); also, it has a reasonably low electron effective mass ($0.4m_0$)[17] comparable to the traditional transparent conductive oxides (ZnO, $In_2O_3$, $SnO_2$). In addition to these favorable charge transport properties, SnO shows intrinsic p-type conduction and extrinsic n-type dopability,[18,19] opening the route to a p-n homojunction solar cell design. The SnO is currently studied as an ambipolar thin film transistor channel material for transparent electronic applications.[20] However, the same optical transparency makes SnO unsuitable as an absorber for solar energy conversion: SnO has an indirect electronic band gap of 0.7 eV and a direct optical band gap of 2.7 eV,[19] despite the high optical absorption coefficient above the optical band gap.[16,21] Thus, improving the optical absorption properties on SnO whilst maintaining good electrical transport properties is one possible approach to design of oxide PV absorbers; it is an interesting alternative to selecting one of the aforementioned transition metal oxides that tend to have better absorption but worse transport.

Recent theoretical calculations suggest that these unfavorable optical properties of SnO can be mitigated by introducing "*structural disorder*" into the cation sublattice by ~10% isovalent alloying on the Sn site with Mg, Zn, Ca, Sr etc, as discussed in more details in Ref. 17. According to the theory, the structural disorder caused by the substitution of these divalent elements weakens the original Sn-O and Sn-Sn bonds leading to an increase of the electronic band gap. At the same time, the reduction of the cation coordination symmetry relaxes the selection rules for the optical transitions between the valence and conduction band leading to a decrease in the optical band gap up to 10% substitution. A similar effect can be achieved by creating mixed Sn valence states in the oxide, as recently suggested by another theoretical study (Ref. 22) Such "*valence*

*disorder*" (as opposed to "*structural disorder*") reduces the $Sn^{2+}$-$Sn^{2+}$ interaction leading to an increase of the electronic band gap and a decrease of the optical band gap, so it is directly related to the $[Sn^{2+}]/[Sn^{4+}]$ oxidation state concentration ratio in the mixed-valent $Sn_xO_y$ oxides.

The main challenge to experimentally realize these theoretical predictions is that the process window for the deposition of phase pure SnO is rather narrow.[23-24] In particular, the formation of SnO is very sensitive to the temperature and the oxygen partial pressure during the synthesis process. Additionally, the 10% substitution of Zn for Sn in $Sn_{1-x}Zn_xO$ constitutes a metastable alloy, since the thermodynamic equilibrium solubility limit is on the order of 1% according to recent calculations.[17] In particular, Zn shows the second highest mixing enthalpy after Mg due to the large ionic radii mismatch. However, taking into account the elemental abundance and the ease of experimental implementation, Zn is still one of the most promising candidate alloying elements for a large-scale fabrication of SnO-based alloys for solar energy conversion applications. The use of metastable alloys in solar energy conversion is not uncommon, for example cation-ordered $GaInP_2$ alloys are used in > 40% efficiency multijunction concentrator photovoltaic devices.[25]

In this paper, we present experimental results of synthesis and characterization of new metastable (Sn,Zn)O alloys with up to 20 cat. at. % Zn substitution as a function of the oxygen partial pressure and substrate temperature during the thin film synthesis. We use a high-throughput parallel experimentation approach to scan a wide range of deposition parameters of the new (Sn,Zn)O alloys in a more comprehensive way than is possible with a conventional serial experimentation approach, identifying the unexpected coupling between the Sn valence state and Zn content. The (Sn,Zn)O thin films with $c_{Zn}/(c_{Sn} + c_{Zn})$ = 10% composition synthesized at optimal deposition conditions determined by this combinatorial study show increased optical absorption in the 1.0-2.0 eV photon energy range. This increase can be tentatively attributed to the theoretically predicted structural disorder introduced by the Zn cation substitution. However, in our experimental samples this effect may be partially masked by the local variations of the Sn valence state predicted by another theoretical study (Ref. 22), which at its extreme may be manifested in light scattering on very small Sn metal precipitates.

## 2. Methods

The experimental exploration of the vast phase space with at least three dimensions (Zn concentration, $O_2$ flow, substrate $T$) by conventional single-point experiments is a large and daunting effort. For such complex problems, the advantage of high-throughput experiments[26] becomes obvious. The high-throughput experiments usually consist of combinatorial film deposition coupled with spatially resolved characterization and followed by automated data analysis. In the case of this (Sn,Zn)O study, crossed gradients of the chemical composition and the substrate temperature on one combinatorial sample library allow for simultaneous exploration of two out of the three dimensions in one deposition experiment. Then, multiple sample libraries are synthesized at different oxygen partial pressures, to cover all three dimensions of the phase space.

Combined with spatially-resolved, semi-automated characterization of composition, structure and optical properties, the narrow process window for the preparation of single-phase (Sn,Zn)O alloys is quickly identified. Subsequently, the (Sn,Zn)O thin film optical properties are studied as a function of composition and structure, to obtain phase pure (Sn,Zn)O material with the desired characteristics for solar cell absorber applications.

The (Sn,Zn)O thin films were deposited by radio-frequency (13.56 MHz) reactive magnetron co-sputtering from two 50 mm metallic targets (purity > 99.993%) in an argon and oxygen containing atmosphere at a pressure of 12 mTorr. The Sn and Zn targets were sputtered for 120 min using 25 W and 15 W power, respectively, leading to the films thicknesses on the order of 500 nm to 2 µm. $Ar/O_2$ volumetric flow ratios of $f_{O2}/(f_{Ar}+f_{O2})$ = 1.75-3.0% and an overall flow of 10 sccm process gas were used. The base pressure of the deposition system was $<5\times10^{-4}$ Pa, and since the system was not equipped with a load lock, it was pumped at least overnight to ensure reproducible growth conditions. As schematically shown in Figure 1, the geometrical arrangement of the two targets (45° tilt with respect to the substrate normal, 140 mm target-substrate distance $d_{ts}$) allowed for the preparation of a continuous compositional gradient between Sn and Zn onto the stationary 2"x2" square Corning EagleXG glass substrates. This composition gradient was orthogonal to the substrate temperature gradient covering ~180°C – 360°C range. The temperature gradient was established by using silver paint to create a strong thermal contact between a quarter of the substrate and the heater, leaving three quarters of the substrate suspended in vacuum.[27,28]

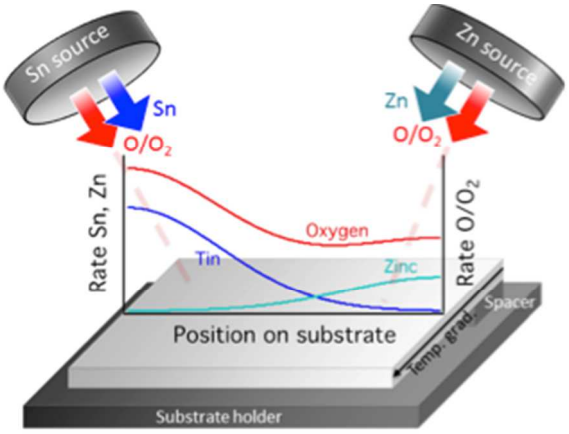


Figure 1: Schematic representation of the combinatorial deposition setup, and the expected variation of the elemental supply rates towards the substrate. It is likely that the variation of the Zn/(Zn+Sn) ratio on the substrate is convoluted with a change in the incoming oxygen flux.

Each 2"x2" combinatorial sample library was characterized at 44 different positions (4x11 grid of samples) for the chemical composition, film thickness, crystallographic structure, and optical absorption on instruments with XY motion stages controlled by computers. The composition and thickness were determined by quantitative X-ray fluorescence measurements (XRF) on a Fischer Scientific (Fischerscope XDV-SDD) instrument using a spot size of 3 mm in diameter. The structure was characterized using a Bruker D8 X-ray diffractometer, equipped with a 2-D detector and a spot size in the order

of 5 mm x 10 mm. The optical transmittance and reflectance were measured in the wavelength range from 300 nm to 1100 nm on a home-built UV/VIS/NIR spectrometer (no integrating sphere) with a spot diameter of approximately 1 mm. The analysis of the resulting large amounts of experimental data was performed using custom written procedures in the Wavemetrics IGOR Pro software package. More details about our implementation of the high-throughput experimental approach can be found in previous publications.[29,30]

For selected samples, transmission electron microscopy (TEM) was performed at 300 kV in an FEI Tecnai $G^2$ 30 S-TWIN TEM for cross-sections prepared using mechanical polishing followed by thinning to electron transparency using low energy (4 kV with final polishing at 1 kV) $Ar^+$ ion milling with the sample stage rotated and cooled by liquid nitrogen. The concentration and mobility of electric charge carriers for the selected samples was measured using Hall effect in 0.3T magnetic field of a permanent magnet. Technical details of theoretical density functional theory (DFT) calculations are exactly the same as described in Ref. 17. Briefly, DFT total energy calculations were performed using projector augmented wave (PAW) method in the VASP code on supercells with special quasi-random structures (SQS). The optical absorption spectra were calculated using modified Becke-Johnson local density approximation (mBJ-LDA), a potential-based meta general gradient approximation (meta-GGA) functional that gives more accurate bandgaps compared to standard DFT.

## 3. Results and Discussion

### 3.1 Chemical exploration of the Sn-Zn-O phase space

To determine the process parameter range for the synthesis of phase pure (Sn,Zn)O alloys in our combinatorial sputtering system, we started by depositing Sn-O thin films without Zn. The oxygen flow during the deposition was chosen to be $f_{O2}/(f_{Ar} + f_{O2})$ = 2.0%, 2.5%, 2.75%, and 3.0% for four combinatorial libraries. Figure 2 shows the resulting phases assigned to the samples on the libraries based on the X-ray diffraction (XRD) data. For low oxygen flows (2%), pure tetragonal SnO (see supporting information for powder diffraction file card numbers) is deposited, while the increased oxygen flow (2.5% and 2.75%) leads to the formation of mixed $SnO/SnO_2$ phases. For the highest studied oxygen flow of $f_{O2}/(f_{Ar} + f_{O2})$ = 3.0%, the films are mostly amorphous. Besides the oxygen flow, the deposition temperature and target-substrate distance $d_{ts,Sn}$ (not shown here) had only a weak influence on the resulting phases. These results are in general agreement with other reports.[23,25,31] We also note that no mixed-valence Sn-O compounds considered by a recent theoretical study[22] have been observed in these synthesis experiments (Fig.2).

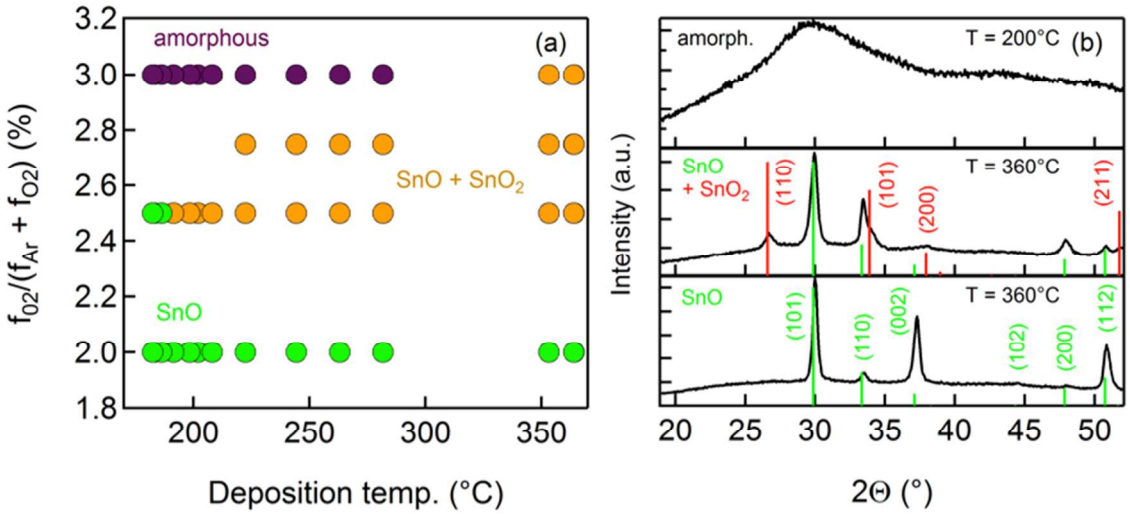


Figure 2: (a) Color map representing the phases/compounds determined from X-ray diffraction on pure Sn-O combinatorial thin film sample libraries, deposited using different oxygen flows and a range of substrate temperatures. (b) Representative XRD pattern of the different phase regions with assigned diffraction peaks according to ICDD reference patterns. Phase pure tetragonal SnO can be synthesized in a wide range of deposition temperatures at low oxygen partial pressures.

Based on the oxygen partial pressure and the substrate temperature used during the synthesis, we calculated the oxygen chemical potential using the ideal gas approximation to be between -0.6…-0.7 eV for the Sn-O thin films prepared with 180°C to 260°C substrate temperature. This value is significantly more positive than the -2.6…-3.0 eV oxygen chemical potential value expected from the theoretically calculated thermodynamic stability diagram of the SnO phase. This shows that the sputtering process parameters used in this study are far away from the extremely reducing conditions required for thermodynamic stability of SnO under equilibrium. Furthermore, from the equilibrium $p_{O2}$-$T$ phase diagrams of the binary Sn-O system, one would expect a *line* rather than a *region* of coexistence of two phases (e.g. SnO and $SnO_2$), in contrast to the experimental observation (Figure 2). Overall the observation of these discrepancies highlights the local non-equilibrium conditions during the sputter deposition of the SnO thin films. This metastable character of sputter deposition can be used for stabilizing (Sn,Zn)O compositions beyond the ZnO solubility range in SnO.

Adding different amounts of Zn during the deposition has a strong influence on the Sn-O phases that form as a function of the substrate temperature and the oxygen flow. Figure 3 shows the phases determined for the combinatorial thin film sample libraries deposited at 1.75%, 2%, 2.25%, 2.5% and 3% oxygen flow. For a given oxygen flow, the oxidation state of the Sn is changing from $Sn^0$ via $Sn^{2+}$ to $Sn^{4+}$ with increasing Zn content in the films (including possibly the mixed-valent $Sn_3O_4$ phase), likely due to increased incident flux of oxygen as explained below. This effect cannot be caused by the increased Sn target substrate distance $d_{ts,Sn}$ (due to the tilted position of the sputtering sources with respect to the substrate surface), since there was no significant change in oxidation state of the tin for the pure Sn-O samples for different $d_{ts,Sn}$. A similar coupling of the oxygen

partial pressure and the cation composition ratio has also been observed in amorphous In-Zn-O alloys,[32] where the amount of oxygen needed to be decreased during the deposition with increasing Zn content, in order to maintain a high conductivity of the thin films. Overall, this leads to an important conclusion for future experimental work by other groups: in order to make phase-pure (Sn,Zn)O films, the oxygen flow needs to be reduced with increasing Zn concentration, compared to the flow used for pure SnO synthesis.

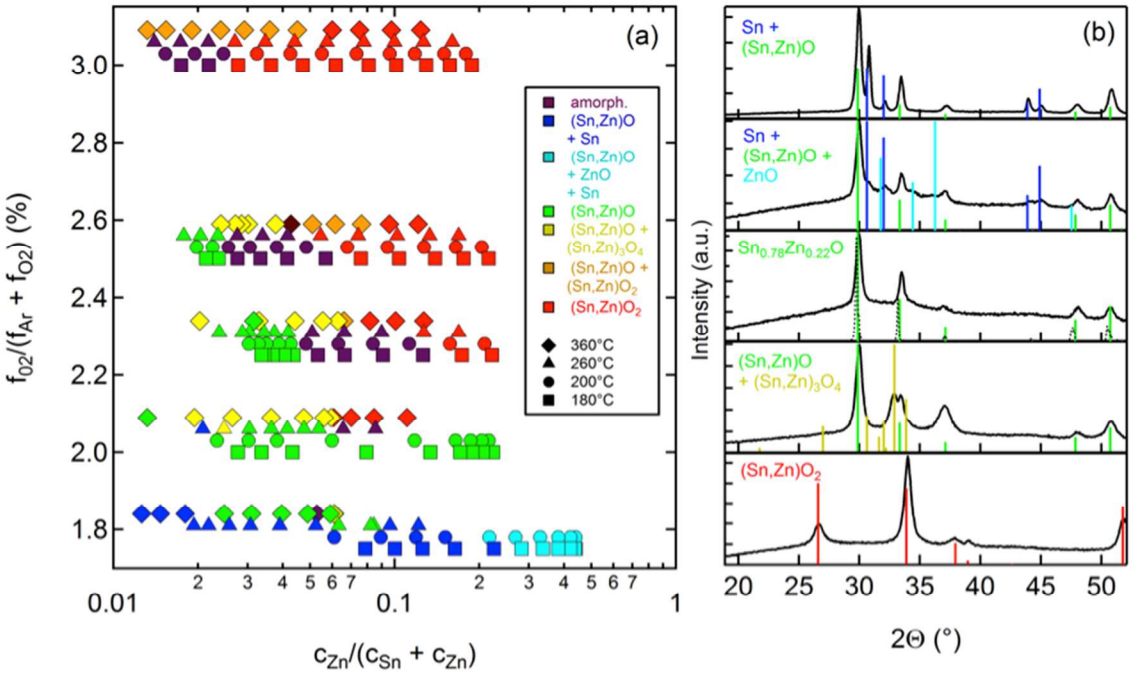


Figure 3: (a) Color map representing the phases/compounds for Sn-Zn-O combinatorial libraries deposited at different oxygen flows, with orthogonal gradients in substrate temperatures and chemical composition. The increasing oxidation of Sn with increasing $c_{Zn}$ can be counteracted by a decreased oxygen flow, leading to phase pure tetragonal (Sn,Zn)O alloys with up to $c_{Zn}/(c_{Sn} + c_{Zn}) \approx 20\%$. The data points for the different temperatures are offset for better visualization. (b) Representative XRD pattern for the different regions on the Sn-Zn-O phase space.

To support our phase assignment for the (Sn,Zn)O alloys, we performed Raman measurements on selected samples (see Figure S1 in supporting information). We were able to identify the Raman signal of SnO (cf. Ref.33) for the samples that showed SnO-like phase by XRD. Moreover, a simulation of the XRD pattern expected for 22% Zn cation concentration (see dotted line in Figure 3 (d) and Figure S2 in supporting information) showed that due to the incorporation of Zn on Sn lattice sites the expected (100) peak shift to lower angles would be ~0.15°. This is the opposite direction of the experimentally observed XRD peak shift, indicating that the chemical stress related to the defects caused by deposition process parameters (temperature, pressure, rate etc.) is dominant for the thin film samples reported in this study. Similar process-dominated stress effects have been previously observed for the sputtered $Cu_{2-2x}Zn_xO$ alloy thin films.[34]

To get a theoretical perspective on the effect of the Zn alloying on the Sn oxidation state in Sn-Zn-O, we calculated the chemical potential phase diagram of the Sn-O system using density functional theory corrected by fitted elemental reference energy (FERE)[35] for SnO and $SnO_2$. The data for the $Sn_3O_4$-like phase (17 meV/atom below convex hull) was taken from literature,[22] where energies for various intermediate Sn-O phases were determined to be 15-19 meV/atom below the SnO-$SnO_2$ convex hull line. Figure 4 shows the regions of stability for the phases present in the Sn-Zn-O alloys as a function of the chemical potential of Sn and O determined from their enthalpies of formation (see Table S2). As shown in Figure 4, the SnO is stable in the $\Delta\mu_O$ = -3.0 … -2.6 eV chemical potential range, which is much more reducing conditions than calculated from the experimental oxygen flow and substrate temperature (see the discussion above). The Sn and $SnO_2$ are stable at lower and higher oxygen chemical potentials, respectively. Between SnO and $SnO_2$, oxides with mixed Sn(II)/Sn(IV) states, such as in $Sn_3O_4$, might be stable.[22]

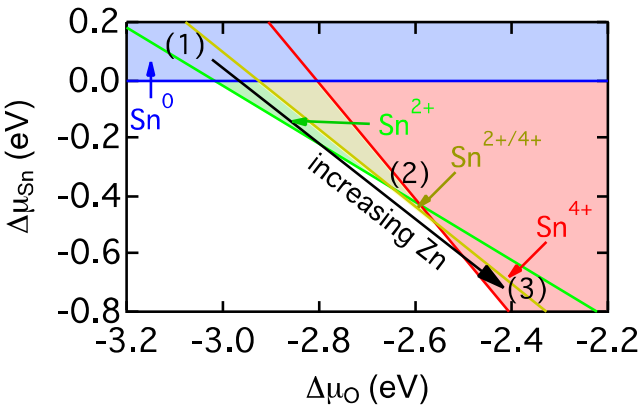


Figure 4: Regions of stability (shaded areas) for Sn, SnO, $SnO_2$ (see Ref. 35), and $Sn_3O_4$ (see Ref. 22) as a function of the oxygen and tin chemical potential. With increasing $c_{Zn}$ in experiment, the oxygen and tin chemical potential increase and decrease, respectively.

The best agreement between the calculated stability regions in Figure 4 and the observed progression of the phases with increasing Zn concentration for a given oxygen flow and deposition temperature in Figure 3, is described by the black arrow in Figure 4, i.e., increasing oxygen and decreasing tin chemical potentials for increasing Zn concentrations. For low zinc concentrations, metallic tin ($Sn^0$) together with (Sn,Zn)O ($Sn^{2+}$) is observed in region (1) of Figure 4, where the tin chemical potential is above 0 eV and the disproportionation of SnO into Sn and $O/O_2$ is likely to be kinetically hindered. As the zinc content increases, pure SnO forms in region (2), and then $SnO_2$ forms in region (3) of Figure 4. For higher oxygen flows during the deposition, the starting point on the arrow is shifted to the right, towards higher oxygen chemical potentials in Figure 4, and the trends with increasing Zn are similar for the entire 180-260 $^oC$ substrate temperature range. At 360$^oC$ substrate temperature, the tin passes a mixture of SnO and $SnO_2$ with increasing zinc concentration, so the phase sequence could correspond to a bottom-right shift of the arrow to lower tin and higher oxygen chemical potentials. Since the oxygen chemical potential is expected to decrease with increasing

temperature in thermodynamic equilibrium,[36] this change is likely due to enhanced (yet incomplete) equilibration of the phases at higher temperature.

The microscopic mechanism of the influence of the Zn on the Sn oxidation state in Sn-Zn-O alloys could tentatively be explained by the "poisoned" character of the target surfaces during the reactive sputtering process. In the poisoned sputtering regime, the consumption of the reactive gas (here $O_2$) by the target is approximately equal to its sputtering rate off the target (here Sn and Zn), while a large portion of the reactive gas is leaving the chamber through the vacuum pump.[37] In this case, the formation of the Sn-Zn-O compound at the substrate is dominated by the oxygen arriving from the target. Figure 1 schematically shows that as the Zn arrival rate from the oxidized Zn target increases with increasing distance from the Sn target ($d_{ts}^{Sn}$), so does the cumulative arrival rate of oxygen from both targets. This larger overall amount of oxygen at the surface of the growing film leads to the formation of more oxidized Sn phases. Thus, it appears that the target substrate distance is an important deposition parameter coupled to Zn concentration. Indeed, the Sn-Zn-O phase diagram re-plotted in $pO_2$-$d_{ts}^{Sn}$ coordinates (Figure S3 in Supporting Information) shows better clustering of the individual phases than the $pO_2$-$c_{Zn}$ phase diagram presented above (Figure 3a).

### 3.2 Optical properties of the (Sn,Zn)O alloys

From the chemical exploration of the Sn-Zn-O phase space presented above, we found that it is possible to counteract the 'oxidizing' effect of the zinc addition on the tin valence state in the (Sn,Zn)O alloy by decreasing the oxygen partial pressure during the deposition. For lower oxygen flows, a higher amount of zinc can be incorporated in the tetragonal SnO phase without phase separation (see green datapoints in Figure 3). In this way, we were able to obtain phase pure (Sn,Zn)O thin films with $c_{Zn}/(c_{Sn} + c_{Zn})$ cation ratios of up to ~20%. However, the films containing more than 10% Zn contained large grains that poorly adhered to the substrate, as evidenced by scanning electron microscopy images presented in Figure S4 of the supporting information. Large grains are beneficial for polycrystalline thin film solar cell applications due to suppressed grain boundary recombination, but they make the characterization of optical properties difficult due to light scattering. On the other hand, smooth and adhering films were achieved for $c_{Zn}/(c_{Sn} + c_{Zn})$ ratios up to ~10%, and the results of their absorption spectra measurements are presented next. We note that these 10-20% compositions are significantly above the thermodynamic solubility limit of Zn in SnO (<1%), which is not uncommon for oxide thin films deposited by non-equilibrium physical vapor techniques.[34,38,39] Above the 10-20% composition, the structure and the properties of the films are more similar to those of Zn-substituted $SnO_2$,[40] and hence are not discussed below.

According to recent theoretical first-principles calculations,[17] the optical band gap of (Sn,Zn)O is expected to be significantly reduced by the introduction of Zn into SnO, as shown in Figure 5c. These calculations assume a constant cation/anion ratio, which implies a constant oxygen chemical potential $\Delta\mu_O$. However, in this work the effective oxygen chemical potential during the sputtering process was shown to depend both on the

zinc concentration and on the oxygen flow (Figure 3). Based on the range where tetragonal (Sn,Zn)O is formed in Figure 3, a contour of constant oxygen chemical potential $\Delta\mu_O(c_{Zn},f_{O2}) \approx$ const. can tentatively be determined, as shown by the dashed lines in Figure 5b.

To determine changes in the optical absorption spectra of the single-phase (Sn,Zn)O alloys prepared with different Zn contents and different oxygen flows during deposition, we performed UV-NIR measurements on our combinatorial sample libraries, and the results are shown in Figure 5 (a) and (b). The absorption coefficient in the 1-2 eV spectral range is increasing with increasing Zn for constant oxygen chemical potential during the growth (Figure 5a). This trend is in a rough quantitative agreement with the theoretical absorption spectra for $c_{Zn}/(c_{Sn} + c_{Zn}) > 2\%$ (Figure 5c) calculated as described in Ref. 17. To quantify these changes, Figure 5 (b) shows as the color scale absorption coefficient averaged for photon energies from 1.75 to 2.0 eV for the phase-pure (Sn,Zn)O alloys. The approximate constant oxygen chemical potential contours that depend on both oxygen flow and zinc content appear in Fig. 5b running at an angle with respect to the coordinate axes. The average absorption increases with increasing Zn content *parallel* to the constant chemical potential contours (without Sn oxidation effects), confirming the theoretical predictions in Ref.17.

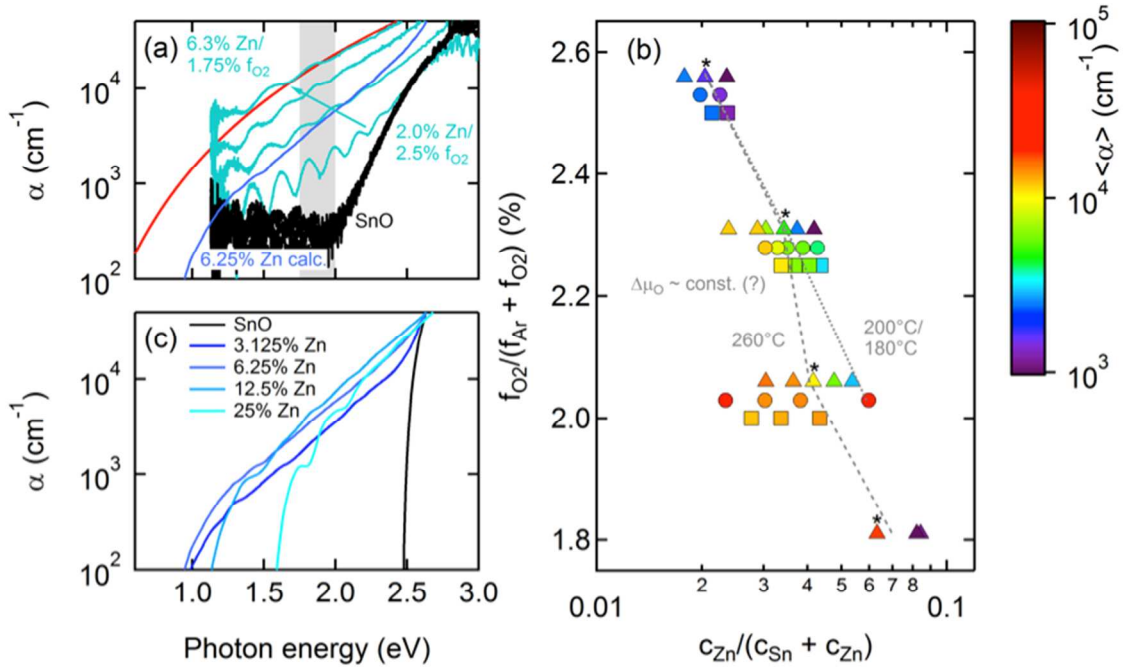


Figure 5: (a) Selected measured (Sn,Zn)O optical absorption spectra ($T_{dep}$ = 260°C). The dark blue line corresponds to first-principles (Sn,Zn)O theoretical predictions, and the red line corresponds to the empirical Sn precipitates model. (b) Measured optical absorption coefficients averaged between 1.75 and 2.0 eV for (Sn,Zn)O films with SnO-like tetragonal structure and smooth surfaces. The diagonal dashed lines approximately correspond to constant chemical potential contours from Figure 3, and the asterisks correspond to the absorption curves in (a). (c) Calculated optical absorption spectra for (Sn,Zn)O with different Zn concentrations, showing first a decrease and then an increase

in the optical bandgap, as predicted by theory.[17] Overall, the figure shows that there is a complex dependence of the absorption coefficient on the zinc content and the oxygen chemical potential during the deposition.

From the experimental Figure 5b, the average absorption also increases with decreasing oxygen chemical potential (decreasing Zn concentration and decreasing oxygen flow), *perpendicular* to the approximate constant oxygen chemical potential lines. Another set of first-principles calculations (Ref.22) recently showed that the optical band gap in intermediate $Sn_xO_y$ oxides is increasing as the $[Sn^{4+}]/[Sn^{2+}]$ concentration ratio is increasing towards higher average Sn oxidation states ranging from SnO to $SnO_2$. Extending this argument, a possible explanation of the increasing absorption perpendicular to the constant oxygen chemical potential lines in Figure 5b could be an increasing tendency to form small precipitates of metallic tin ($Sn^0$) that may not be detectable by XRD (Figure 3) and Raman (Figure S1). These small metallic particles could lead to absorption and/or scattering of the light, both of which could decrease the forward amplitude of the measured light.

The expected strong wavelength dependence of the scattering contribution ($\lambda^{-4}$) to the apparent absorption coefficient fits well the observed dispersion of the measured absorption coefficients with the photon energy (see red curve in Figure 5a). The apparent absorption coefficient due to the scattering process is determined by the equation

$$\alpha_{sca} = 128\pi^4 r^3 f \left(\frac{n_m}{\lambda_{vac}}\right)^4 \left|\frac{\frac{\tilde{\varepsilon}_{inc}}{\tilde{\varepsilon}_m} - 1}{\frac{\tilde{\varepsilon}_{inc}}{\tilde{\varepsilon}_m} + 2}\right|^2$$

with the radius of the spherical inclusions $r$, the real part of the complex refractive index of the medium $n_m$, the wavelength of the light in vacuum $\lambda_{vac}$, and the complex dielectric functions of the inclusions, $\tilde{\varepsilon}_{inc}$, as well as the medium, $\tilde{\varepsilon}_m$. This formula can be derived from the elastic scattering cross section $c_{sca}$ of small spherical particles ($x << 1$, $x = n_m k_{vac} r$) that has been previously described by Rayleigh (Ref. 41), using $\alpha = N_{inc} c_{sca}$ to relate the scattering cross section $c_{sca}$ to the density of inclusions $N_{inc}$, and using $f = 4/3\pi r^3 N_{inc}$ to relate $N_{inc}$ to their volume fraction $f$.

To get a deeper experimental insight into the relative contributions of the "structural disorder" (Ref. 17) and "valence disorder" (Ref. 22) to the increase of the apparent optical absorption (Figure 5), we investigated the micro- and nanostructure of the (Sn,Zn)O thin films by transmission electron microscopy (TEM) measurements. As shown in bright field TEM image in Figure 6a, the (Sn,Zn)O films with 2.4% Zn and enhanced optical absorption compared to SnO (Figure 5a) have columnar structure typical of sputtered oxide films, with an average grain size of <100 nm; similar results have been obtained for the 4% Zn sample. The lattice plane spacing measured from the transmission electron diffraction (TED) patterns (Figure 6a inset) is consistent with the tetragonal SnO phase; no bulk precipitates of secondary phases have been observed in the bulk of the (Sn,Zn)O thin film. This supports the hypothesis that the observed optical

absorption effects in Figure 5 comes at least in part from the intrinsic "structural disorder" effect predicted by first principles calculations.[17]

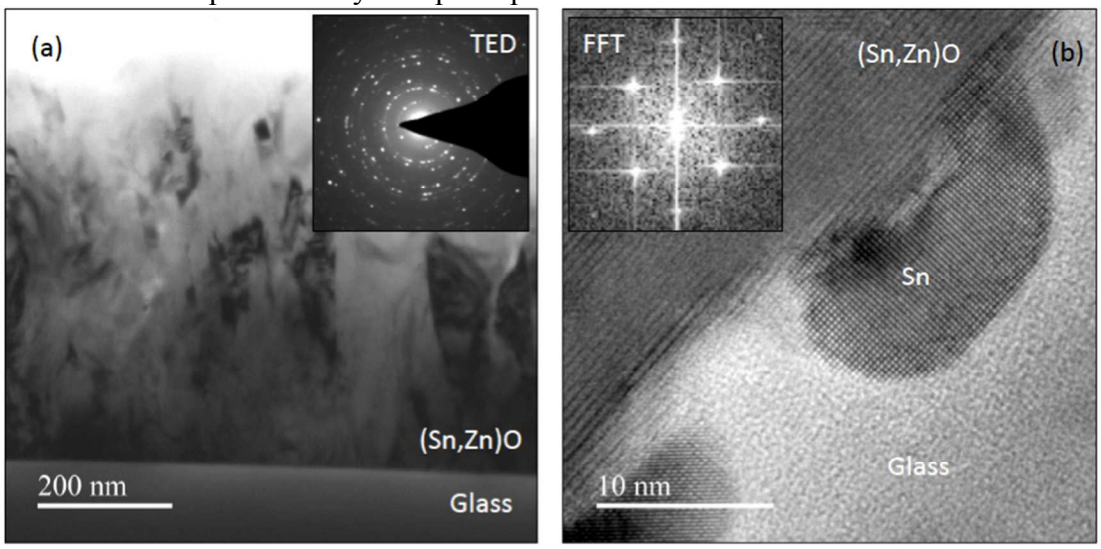


Figure 6: (a) Bright field TEM image of the (Sn,Zn)O film with typical 100 nm columnar grains on glass, with transmission electron diffraction characteristic of SnO structure shown in the inset. (b) The HRTEM image of the interface between the SnO film and the glass substrate in the region where a 10 nm Sn interface particle has been identified after 15 hours low energy $Ar^+$ ion milling. The FFT of the particle region is shown in the inset.

Figure 6b shows the interface between the SnO film and the glass substrate for a sample that has 2.4% Zn content and an enhanced optical absorption onset compared to SnO (Figure 5a). The high-resolution TEM (HRTEM) results indicate the presence of a precipitated material in the interfacial layer between the glass substrate and the (Sn,Zn)O film with 2.4% Zn (the same for 4% Zn, not shown here). The measured lattice spacings of this material with cubic or tetragonal structure are ≈2.05 Å and ≈2.89 Å, which is consistent with $d_{220}$ (2.06 Å) and $d_{020}$ (2.91 Å) of tetragonal β-Sn. In addition, STEM HAADF imaging and EDS mapping (not shown) confirm that these interface particles are Sn-rich. The size of these Sn particles (10-20 nm) are consistent with the assumptions of the Rayleigh scattering (Ref. 38), so in principle they can cause the optical effect observed in Figure 5. However, since these particles are very small and observed only in the top layer of the glass and not in the bulk of the film, they may be related to the difficulties in controlling the very low oxygen flow at the initial stages of the deposition. It is also possible but less likely that these particles are caused by the over 15 hours of low energy (< 4 kV) $Ar^+$ ion milling, required to thin the samples to electron transparency, since the samples were mounted on a rotating, liquid nitrogen cooled stage to reduce any artifacts due to sample heating during the ion milling process.. More detailed microscopy studies would be required to clearly distinguish between these two possibilities. In addition, synchrotron-based x-ray absorption spectroscopy (XAS), x-ray photoelectron spectroscopy (XPS), or electron energy loss spectroscopy (EELS) would be advantageous to study the oxidation state of Sn in (Sn,Zn)O in the future.

Finally, we briefly discuss the electrical doping and charge transport properties of the (Sn,Zn)O alloys. The results of the Hall effect measurements indicate that both Zn-free and Zn-containing samples have p-type conduction with hole mobility of 0.2-0.4 $cm^2/Vs$, which may be attributed either to scattering on ionized defects or on grain boundaries. This suggests that the defect concentration needs to be decreased and grain size needs to be increased, by carefully controlling the process conditions[31] to make these alloys more suitable for solar energy conversion applications. However, the hole concentration in Zn-containing samples is $1x10^{19}$ $cm^{-3}$, which is 10-20x higher compared to the Zn-free samples $5x10^{18}$ $cm^{-3}$ - $1x10^{18}$ $cm^{-3}$. These results are consistent with the earlier discussion that addition of Zn to SnO has an oxidizing effect, leading to lowering of the Fermi level and increasing hole concentration. More detailed studies of the (Sn,Zn)O electrical doping and transport properties are in progress and will be reported in future publications.

## 4. Summary and Conclusions

In summary, the addition of Zn to SnO during the Sn-Zn-O synthesis induces a change of the Sn valence state from $Sn^0$ via $Sn^{2+}$ to $Sn^{4+}$, which can be counteracted by reducing the oxygen partial pressure in the sputtering atmosphere. These results can be explained by changes in the effective oxygen chemical potential at the substrate in the 'poisoned' regime of reactive sputtering used in this work. By simultaneously adjusting the zinc and the oxygen content, we were able to prepare small-grain well-adhering phase-pure metastable heterostructural (Sn,Zn)O alloys with up to $c_{Zn}/(c_{Sn} + c_{Zn}) = 10\%$ in the tetragonal SnO-like structure, and for phase-pure (Sn,Zn)O films with up to 20% Zn content and with large grains and poor adhesion to the glass substrate. The analysis of the optical properties of the smooth (Sn,Zn)O thin films showed an increase of the absorption coefficient in the energy range from 1 to 2 eV. The observed optical absorption effects can be explained by two general mechanisms: (1) a change of the optical absorption caused by a modification of the band structure due to isovalent alloying (structural disorder), [17] and (2) a change in absorption due to the modification of local mixed Sn valence states shifting the electronic bands (valence disorder) [22]. The electron microscopy attempts discussed in this study show that both of these mechanisms can contribute to the observed optical absorption changes.

By means of conclusion, it would be necessary to prepare in the future (Sn,Zn)O samples with exactly the same mean and the same distribution of Sn oxidation states for different Zn concentrations. Such samples would allow one to separate the effects of the valence disorder due to local variation of the mixed Sn oxidation state in Sn-O, from the effect of the structural disorder due to incorporation of Zn on Sn lattice sites in (Sn,Zn)O. This high-throughput experimental study paves the way to such quantitative comparison between the experimental results and the theoretical predictions, by identify synthesis conditions where phase-pure (Sn,Zn)O samples can be grown using conventional (non-combinatorial) experimental techniques. Furthermore, a more detailed microscopy analysis would be necessary in the future, to ensure that the Zn is actually incorporated on the Sn lattice sites, due to the high mixing enthalpy of SnO and ZnO. If the Zn substitution for Sn is found problematic, SrO or CaO could be alloyed with SnO, since

they have been predicted to have less positive mixing enthalpies due to a better ionic size match of Ca and Sr with Sn.[17] Such (Sn,M)O alloys would be promising oxide absorber candidates for large-scale photovoltaic and photoelectrochemical solar energy conversion applications.

**Supporting Information**

XRD reference pattern numbers
Materials formation enthalpies
Measured Raman spectra
Simulated XRD patterns
Materials phase maps
SEM images of films

**Acknowledgements**

This work was supported by the U.S. Department of Energy, Office of Energy Efficiency and Renewable Energy, under Contract No. DE-AC36-08-GO28308 with the National Renewable Energy Laboratory, as a part of the SunShot initiative.

**References**

[1] C. Wadia, A.P. Alivisatos, and D.M. Kammen, Materials availability expands the opportunity for large-scale photovoltaics deployment, *Environ. Sci. Technol*. 2009, *43*, 2072-2077

[2] A. Walsh, S. Chen, S.H. Wei, and X.G. Gong, Kesterite Thin-Film Solar Cells: Advances in Materials Modelling of $Cu_2ZnSnS_4$, *Adv. Energy Mater*. 2012, *2*, 400-409.

[3] J.R. McKone, N.S. Lewis, and H.B. Gray, Will solar-driven water-splitting devices see the light of day?, *Chem. Mater.* 2014, *26*, 407-414

[4] M.A. Green, Photovoltaic principles, *Phys. E Low-Dimensional Syst. Nanostructures* 2002, *14*, 11-17.

[5] S. Rühle, A.Y. Anderson, H.N. Barad, B. Kupfer, Y. Bouhadana, E. Rosh-Hodesh, and A. Zaban, All-oxide photovoltaics, *J. Phys. Chem. Lett.* 2012, *3*, 3755-3764..

[6] B.K. Meyer, A. Polity, D. Reppin, M. Becker, P. Hering, P.J. Klar, T. Sander, C. Reindl, J. Benz, M. Eickhoff, C. Heiliger, M. Heinemann, J. Bläsing, A. Krost, S. Shokovets, C. Müller, and C. Ronning, Binary copper oxide semiconductors: from materials towards devices, *Phys. Status Solidi* 2012, *249*, 1487-1509.

[7] B.P. Rai, $Cu_2O$ solar cells: a review, *Sol. Cells* 1988, *25*, 265-272

[8] B. Kupfer, K. Majhi, D.A. Keller, Y. Bouhadana, S. Rühle, H.N. Barad, A.Y. Anderson, and A. Zaban, Thin Film $Co_3O_4/TiO_2$ Heterojunction Solar Cells, *Adv. Energy Mater*. 2015, 5, 1401007.

[9] R. Nechache, C. Harnagea, S. Li, L. Cardenas, W. Huang, J. Chakrabartty, and F. Rosei, Bandgap tuning of multiferroic oxide solar cells, *Nat. Photonics* 2015, *9*, 61-67.

[10] W. Smith and Y. Zhao, Enhanced photocatalytic activity by aligned $WO_3/TiO_2$ two-layer nanorod arrays, *J. Phys. Chem. C* 2008, *112*, 19635-19641

[11] K. Sivula, F. Le Formal, and M. Grätzel, $WO_3-Fe_2O_3$ photoanodes for water splitting: A host scaffold, guest absorber approach, *Chem. Mater.* 2009, *21*, 2862-2867.

[12] K. Sivula, F. Le Formal, and M. Grätzel, Solar water splitting: progress using hematite (α-$Fe_2O_3$) photoelectrodes, *ChemSusChem* 2011, *4*, 432-449
[13] Y. Liang, T. Tsubota, L.P.A. Mooij, and R. Van De Krol, Highly improved quantum efficiencies for thin film $BiVO_4$ photoanodes, *J. Phys. Chem. C* 2011, *115*, 17594-17598.
[14] Q. Yan, G. Li, P.F. Newhouse, J. Yu, K.A. Persson, J.M. Gregoire, and J.B. Neaton, High Throughput Discovery of Solar Fuels Photoanodes in the CuO–$V_2O_5$ System, *Adv. Energy Mater.* 2015, 5, 1401840.

[15] H.S. Stein, R. Gutkowski, A. Siegel, W. Schuhmann, and A. Ludwig, New materials for the light-induced hydrogen evolution reaction from the Cu–Si–Ti–O system, *J. Mater. Chem. A* 4, 2016, *4*, 3148-3152.
[16] Q.-J.J. Liu, Z.-T.T. Liu, and L.-P.P. Feng, First-principles calculations of structural, electronic and optical properties of tetragonal $SnO_2$ and SnO, *Comput. Mater. Sci.* 2010, *47*, 1016-1022.
[17] H. Peng, A. Zakutayev, S. Lany, Tuning Optical Absorption of SnO by Isoelectronic Alloying for PV Absorber *arXiv*: 1504.01168 (2015).

[18] N.F. Quackenbush, J.P. Allen, D.O. Scanlon, S. Sallis, J.A. Hewlett, A.S. Nandur, B. Chen, K.E. Smith, C. Weiland, D.A. Fischer, J.C. Woicik, B.E. White, G.W. Watson, and L.F.J. Piper, Origin of the bipolar doping behavior of SnO from X-ray spectroscopy and density functional theory, *Chem. Mater.* 2013, *25*, 3114-3123.
[19] H. Hosono, Y. Ogo, H. Yanagi, and T. Kamiya, Bipolar conduction in SnO thin films, *Electrochem. Solid-State Lett.* 2011, *14*, H13-H16.
[20] K. Nomura, T. Kamiya, and H. Hosono, Ambipolar oxide thin-film transistor, *Adv. Mater.* 2011, *23*, 3431-3434.
[21] L.Y. Liang, Z.M. Liu, H.T. Cao, Y.Y. Shi, X.L. Sun, Z. Yu, A.H. Chen, H.Z. Zhang, and Y.Q. Fang, Improvement of phase stability and accurate determination of optical constants of SnO thin films by using $Al_2O_3$ capping layer, *ACS Appl. Mater. Interfaces* 2010, *2*, 1565-1568.
[22] J. Wang, N. Umezawa, and H. Hosono, Mixed Valence Tin Oxides as Novel van der Waals Materials: Theoretical Predictions and Potential Applications, *Adv. Energy Mater.* 1501190 (2015).

[23] E. Leja, T. Pisarkiewicz, and A. Kolodziej, Electrical properties of non-stoichiometric tin oxide films obtained by the dc reactive sputtering method, *Thin Solid Films* 1980, *67*, 45-48.
[24] H. Luo, L.Y. Liang, H.T. Cao, Z.M. Liu, and F. Zhuge, Structural, chemical, optical, and electrical evolution of $SnO_x$ films deposited by reactive rf magnetron sputtering, *ACS Appl. Mater. Interfaces* 2012, *4*, 5673-5677.
[25] S. Froyen, and A. Zunger, Surface-induced ordering in GaInP. *Physical Review Letters*, 1991, *66*, 2132.
[26] M.L. Green, I. Takeuchi, and J.R. Hattrick-Simpers, Applications of high throughput (combinatorial) methodologies to electronic, magnetic, optical, and energy-related materials, *J. Appl. Phys.* 2013, *113*, 231101.
[27] A. Subramaniyan, J.D. Perkins, R.P. O'Hayre, S. Lany, V. Stevanovic, D.S. Ginley, and A. Zakutayev, Non-equilibrium deposition of phase pure $Cu_2O$ thin films at reduced growth temperature, *APL Mater.* 2014, *2*, 022105.

[28] C.M. Caskey, R.M. Richards, D.S. Ginley, and A. Zakutayev, Thin film synthesis and properties of copper nitride, a metastable semiconductor, *Mater. Horizons* 2014, *1*, 424-430.
[29] A.W. Welch, P.P. Zawadzki, S. Lany, C.A. Wolden, and A. Zakutayev, Self-regulated growth and tunable properties of $CuSbS_2$ solar absorbers, *Sol. Energy Mater. Sol. Cells* 2014, *132*, 499-506.
[30] A. Zakutayev, F.J. Luciano, V.P. Bollinger, A.K. Sigdel, P.F. Ndione, J.D. Perkins, J.J. Berry, P.A. Parilla, and D.S. Ginley, Development and application of an instrument for spatially resolved Seebeck coefficient measurements, *Rev. Sci. Instrum*. 2013, *84*, 053905.
[31] J.A. Caraveo-Frescas, P.K. Nayak, H.A. Al-Jawhari, D.B. Granato, U. Schwingenschlögl, and H.N. Alshareef, Record mobility in transparent p-type tin monoxide films and devices by phase engineering, *ACS Nano* 2013, *7*, 5160-5167.
[32] J.D. Perkins, M.F.A.M. Van Hest, M.P. Taylor, and D.S. Ginley, Conductivity and transparency in amorphous In-Zn-O transparent conductors, *Int. J. Nanotechnol*. 2009, *6*, 850-859.
[33] J. Geurts, S. Rau, W. Richter, and F.J. Schmitte, SnO films and their oxidation to $SnO_2$: Raman scattering, IR reflectivity and X-ray diffraction studies, *Thin Solid Films* 1984, *121*, 217-225.
[34] A. Subramaniyan, J.D. Perkins, R.P. O'Hayre, D.S. Ginley, S. Lany, and A. Zakutayev, Non-equilibrium synthesis, structure, and opto-electronic properties of $Cu_{2-2x}Zn_xO$ alloys, *J. Mater. Sci.* 2015, *50*, 1350-1357.
[35] V. Stevanovic, S. Lany, X. Zhang, and A. Zunger, Correcting density functional theory for accurate predictions of compound enthalpies of formation: Fitted elemental-phase reference energies, *Phys. Rev. B* 2012, *85*, 115104
[36] E. Heifets, E. Kotomin, Y. Mastrikov, S. Piskunov, and J. Maier, in *Thermodynamics - Interaction Studies - Solids, Liquids, Gases* (InTech, 2011).
[37] S. Berg and T. Nyberg, Fundamental understanding and modeling of reactive sputtering processes, *Thin Solid Films* 2005, *476*, 215-230.
[38] V. Stevanović, A. Zakutayev, and S. Lany, Composition Dependence of the Band Gap and Doping in $Cu_2O$-Based Alloys as Predicted by an Extension of the Dilute-Defect Model, *Phys. Rev. Appl.*, 2014, *2*, 044005
[39] H. Peng, P.F. Ndione, D.S. Ginley, A. Zakutayev, and S. Lany, Design of Semiconducting Tetrahedral $Mn_{1-x}Zn_xO$ Alloys and Their Application to Solar Water Splitting, *Phys. Rev. X,* 2015, *5*, 021016.
[40] X. Dou, D. Sabba, N Mathews, L.H. Wong, Y.M. Lam, and S. Mhaisalkar, S., Hydrothermal synthesis of high electron mobility Zn-doped $SnO_2$ nanoflowers as photoanode material for efficient dye-sensitized solar cells. *Chemistry of Materials*, *2011, 23*, 3938-3945.
[41] D.D. Nolte, Optical scattering and absorption by metal nanoclusters in GaAs, *J. Appl. Phys.* 1994, *76*, 3740-3745.